

The shapes of AGB envelopes as probes of binary companions

P. J. Huggins^{1*}, N. Mauron², and E. A. Wirth¹ ^{*}†

¹*Physics Department, New York University, 4 Washington Place, New York NY 10003, USA*

²*GRAAL, CNRS, and Université Montpellier II, Place Bataillon, 34095 Montpellier, France*

Accepted ... Received; in original form ...

ABSTRACT

We describe how the large scale geometry of the circumstellar envelopes of asymptotic giant branch stars can be used to probe the presence of unseen stellar companions. A nearby companion modifies the mass loss by gravitationally focusing the wind towards the orbital plane, and thereby determines the shape of the envelope at large distances from the star. Using available simulations, we develop a prescription for the observed shapes of envelopes in terms of the binary parameters, envelope orientation, and type of observation. The prescription provides a tool for the analysis of envelope images at optical, infrared, and millimetre wavelengths, which can be used to constrain the presence of companions in well observed cases. We illustrate this approach by examining the possible role of binary companions in triggering the onset of axi-symmetry in planetary nebula formation. If interaction with the primary leads to axi-symmetry, the spherical halos widely seen around newly formed nebulae set limits on the companion mass. Only low mass objects may orbit close to the primary without observable shaping effects: they remain invisible until the interaction causes a sudden change in the mass loss geometry.

Key words: stars: AGB and post-AGB – stars: mass loss – binaries: close – planetary nebulae: general

1 INTRODUCTION

One of the striking aspects of the evolution of stars from the asymptotic giant branch (AGB) to the planetary nebula (PN) phase is the sudden change in morphology of the circumstellar gas. On the AGB, the stellar mass loss is thought to be roughly spherically symmetric, but this rapidly evolves into prominent axi-symmetry on evolution into the proto-PN phase. The axial symmetry may consist of a smooth gradient in mass loss from pole to equator or a distinct equatorial torus, and is often accompanied by high velocity bi-polar or multi-polar jets, aligned approximately along the symmetry axis.

Most of the theoretical ideas that have been proposed to explain the axi-symmetry rely on the presence of a binary companion. There is, however, no consensus on a specific scenario, and exactly what happens is controversial. Proposals include tidal effects; engulfment of the compan-

ion with expulsion of a common envelope; and the effects of jets, from accretion disks around the companion or around the core of the primary (e.g., Morris 1987; Soker & Livio 1994; Reyes-Ruiz & López 1999; Soker & Rappaport 2000; Nordhaus & Blackman 2006).

If the axial symmetry of PNe is due to the effects of a binary companion, the relatively common occurrence of this phenomenon (e.g., Sahai et al. 2007) strongly constrains the possible star systems that become PNe. However, the observational situation with respect to binarity is not clear. Relatively few AGB stars are known to have binary companions (Jorissen 2003, Table 9.1). Unless the companion is bright or hot, it is difficult to detect given the high luminosity and variability of the primary and its thick circumstellar envelope. The central stars of PNe are somewhat more accessible targets, and extensive searches have been made for companions using photometry, imaging, and radial velocity measurements (e.g., de Marco 2006; Miszalski et al. 2009). However, only a few dozen cases with companions have been found. These are typically short period systems which imply direct interaction in the past, but the general issue of PN formation remains an open question, especially in view

* E-mail: patrick.huggins@nyu.edu (PJH); mauron@graal.univ-montp2.fr (NM); eaw300@nyu.edu (EAW)

† Based in part on data from the NASA/ESA/CADC HST archives, and the ESO VLT archive.

of the difficulty in finding companions with intermediate or long periods.

In this paper we discuss a different approach for probing the presence of a binary companion that might affect the AGB–PN transition. It is based on the influence of the companion in shaping the mass loss of the AGB star before the transition takes place. The shaping effect is frozen into the expanding circumstellar envelope, and is reflected in its large scale geometry.

This approach is possible because changes in the separation of the system are reasonably well prescribed. In cases where the companion comes into contact with or is engulfed by the AGB star during the transition, it must initially have been relatively close, within several AU. If the companion induces the transition from somewhat farther out, the orbital separation is expected to undergo a slow increase in response to the mass loss of the system. In all cases where the companion significantly affects the transition, it is likely to be well within the circumstellar envelope during the AGB phase, and can be expected to affect the large scale geometry of the envelope over a long time period. The geometry of the extended envelope can be studied with a variety of techniques on the AGB. It can also be studied in the halos of proto-PNe and PNe, in material that was ejected earlier by the AGB star and lies outside the developing axi-symmetric nebula.

The plan of the paper is as follows. In the next section we discuss the effects of detached binary companions on the large scale geometry of AGB envelopes. We then develop a prescription for the observed shapes of the envelopes in terms of the binary parameters and the orientation. We illustrate how these results can be used to probe the presence of companions by measuring the shape in well-studied cases, and we discuss some implications for the formation of PNe.

2 SHAPING EFFECTS OF AN AGB COMPANION

There are no systematic observations of the extended envelopes of AGB stars with companions, although there are a few cases known in which strong interactions already appear to be taking place. For example, π^1 Gru shows an equatorial torus and jets, similar to the configuration seen in proto-PNe (e.g., Chiu et al. 2006; Sacuto et al. 2008; Huggins 2007). We therefore rely on numerical simulations to understand the effects of a companion on the large scale structure (Theuns & Jorissen 1993; Mastrodemos & Morris 1999 [hereafter MM99]; Gawryszczak et al. 2002). The available simulations are not very extensive, but the general nature of the effects caused by the companion is clear. In addition to local interactions which may include tidal spin-up of the primary and accretion of envelope material by the secondary, there are two main effects on the extended circumstellar envelope.

First, for a wide range of conditions, a spiral pattern is imprinted on the envelope, mainly as a result of the reflex motion of the primary. An example of this has been detected in the envelope of the evolved carbon star AFGL 3068 (Mauron & Huggins 2006; Morris et al. 2006). The spiral formed by this mechanism is not easy to detect. The radial wavelength of the pattern (λ) is given by $\lambda = VP$, where

V is the expansion velocity of the envelope, and P is the period of the binary. Even for relatively nearby AGB stars the pattern is resolvable only for long periods. In the case of AFGL 3068 the period is ~ 800 yr and the corresponding separation ~ 100 AU, which is probably too large for the companion to play an important role in the AGB-PN transition.

The second effect of a companion on the extended envelope is to modify the mass loss geometry by gravitationally focusing matter towards the orbital plane. The latitude-density profile is eventually frozen into the wind flow at the terminal velocity in each direction, and this results in a flattened large scale structure. The evolutionary time scale on the AGB is much longer than the binary orbital periods of interest here, so the spiral pattern, if present, forms a fine structure on the extended envelope. Averaged over many spiral features, the large scale structure provides a probe of the presence of the companion, with a characteristic size scale much larger than the binary separation or the spiral pattern. It is this large scale structure that we quantify in the following sections.

3 THE ENVELOPE SHAPE

3.1 Characterising the shape

We develop an approximate prescription for the large scale binary shaping of AGB envelopes based on the binary simulations of MM99, which are the most comprehensive. Details of the numerical techniques, physical assumptions, and limitations of the simulations are discussed at length by Mastrodemos (1998). The models we use are listed in Table A1. They employ a single primary mass of $1.5 M_{\odot}$ with mass loss rates $\sim 1\text{--}2 \times 10^{-5} M_{\odot} \text{ yr}^{-1}$ appropriate for AGB stars. The parameter space covers $0.25\text{--}2.0 M_{\odot}$ for the secondary mass (M_s), $3.6\text{--}50.4$ AU for the binary separation (d), and $5\text{--}17 \text{ km s}^{-1}$ for the wind velocity at the location of the secondary (V_s). The wind from the star is assumed to be initially spherically symmetric. A close-in secondary may spin-up the primary or cause other effects which may enhance equatorial mass loss. In this sense the simulations provide a lower limit to the actual degree of axi-symmetry.

The overall shapes of the envelopes affected by gravitational focusing vary from model to model, depending on the parameters of the binary. For high mass, close-in companions, the wind is highly concentrated towards the orbital plane, and for lower mass, more distant companions the flow is more spherically symmetric. At large distances from the star system where the wind is in steady state at the terminal velocity, the latitude variation of the density is frozen into the flow.

We characterise the latitude variation of density in the extended envelope using an exponential profile. The density is then given by the equation:

$$n(r, \theta) = \frac{n_a r_a^2}{r^2} \exp(-\theta/\theta_o), \quad (1)$$

where the r is the distance from the centre, n_a is the equatorial density at reference radius r_a , θ is the latitude (measured from the orbital plane in degrees), and θ_o is the scale height. The exponential profile is adopted as a simple approximation to the actual latitude variation of the five simulations

reported by MM99 in their Fig. 23 and Table 3. These profiles differ in detail from model to model; the procedure used below matches them to an exponential at the orbital plane and at intermediate latitudes. For the most flattened envelope (model 1), the approximation is not an accurate fit of the detailed profile near the plane: the mean (absolute) deviation (averaged over latitude 0° – 85°) is 0.19 dex. In this case however, the total variation in density from pole to equator is extremely large, more than a factor of 300 (2.6 dex), so the approximation is still a useful descriptor of the overall shape. For the less flattened envelopes, which are the main focus of later discussion, the procedure provides quite good approximations to the detailed profiles. For example, for model 3, the exponential differs from the exact profile by a mean (absolute) deviation of 0.03 dex.

To determine the value of θ_o for each simulation in Table A1 we fit equation (1) to the ratio of the density at the equator and intermediate latitudes 50° and 80° , and adopt the geometric mean. The dispersion of the individual estimates about the adopted values is 10% (rms).

A shape parameter equivalent to θ_o is the density contrast $(n_{\text{eq}} - n_{\text{po}})/n_{\text{po}}$, where n_{eq} and n_{po} are the densities at the equator and poles, at the same radial distance. It is convenient to write the contrast as $K_n - 1$ where K_n is the equator/pole density ratio, i.e.,

$$K_n - 1 = (n_{\text{eq}} - n_{\text{po}})/n_{\text{po}}. \quad (2)$$

This is zero for a spherical envelope, and increases with the degree of flattening. For the exponential model, it is seen from equation (1) that K_n and θ_o are related by the expression $K_n = \exp(90/\theta_o)$. These simple characterisations are used to represent the overall shape of each envelope.

3.2 Relation to binary parameters

The next step in our prescription is to determine an empirical relation between the binary parameters and the envelope shape, using the density contrast $K_n - 1$ introduced above. We follow in part the earlier discussion by MM99.

In order to guide the analysis, we assume that the gravitational focusing depends only on the following parameters: the masses of the primary and secondary (M_p and M_s), the separation (d), and the velocity of the wind at the orbit of the secondary (V_s). We ignore the possible influence of other quantities such as the dimensions of the stars, the form of the wind acceleration curve, etc., which we assume to be of secondary importance. It then follows from dimensional analysis that the density contrast $K_n - 1$ depends on a function Φ of at most two dimensionless combinations of the independent variables and the gravitational constant G .

In certain limiting cases, physical arguments provide further information on the form of Φ . For example, in the limit that $V_o \ll V_s$, where V_o is the orbital velocity ($V_o^2 = G(M_p + M_s)/d$), the trajectories of the wind particles in the ballistic limit scale with only one dimensionless parameter, $GM_s/V_s^2 d$. Similarly, in the limit of large M_p where the orbital velocity is large, the presence of the secondary acts effectively as a thin ring, and the contrast again depends on the same dimensionless parameter. In the intermediate regime of interest here, the situation is less amenable to simple analysis, but the above considerations motivate a parameterisation of the form:

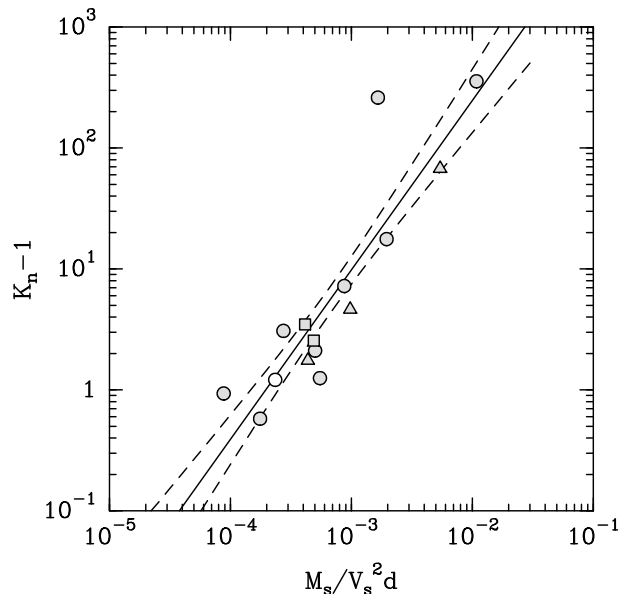


Figure 1. Envelope shape parameter $K_n - 1$ vs. binary parameters $M_s/V_s^2 d$, in units of $M_\odot/(\text{km s}^{-1})^2 \text{AU}$. The symbols show model data from Table A1 and indicate the value of the parameter $1 + M_p/M_s$: open circles (1.75), filled circles (2.5), triangles (4.0), and squares (7.0). The solid line is the least squares fit to the data, and the dashed lines are one-sigma confidence limits of the fit.

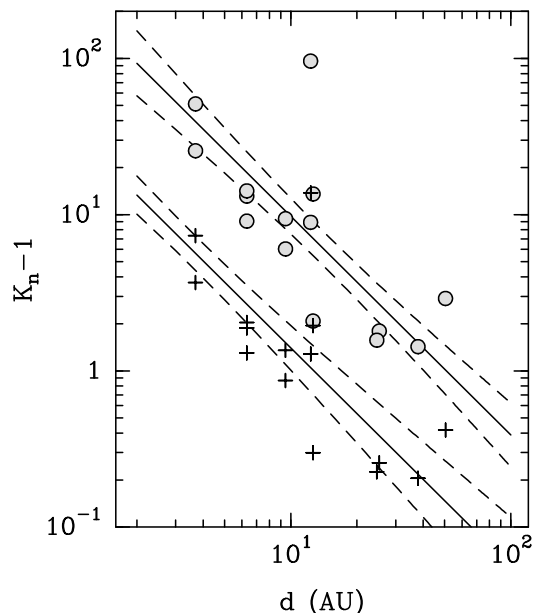


Figure 2. Envelope shape parameter $K_n - 1$ vs. separation d , projected from Fig. 1 for $V_s = 10 \text{ km s}^{-1}$. The upper lines and circles are for $M_s = 1 M_\odot$; the lower lines and crosses are for $M_s = 0.25 M_\odot$.

$$K_n - 1 = \Phi(GM_s/V_s^2 d, (M_p + M_s)/M_s). \quad (3)$$

From the numerical results of the simulations, it is found that $K_n - 1$ shows a strong dependence on the first parameter in equation (3). The data are shown in Fig. 1. The variation is well approximated by a power law, and a least squares fit gives:

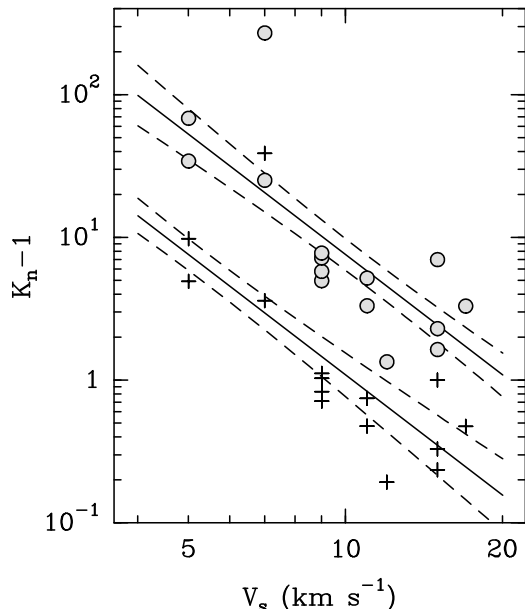


Figure 3. Envelope shape parameter $K_n - 1$ vs. wind velocity V_s , projected from Fig. 1 for separation $d = 12$ AU. The upper lines and circles are for $M_s = 1 M_\odot$; the lower lines and crosses are for $M_s = 0.25 M_\odot$.

$$\log(K_n - 1) = 5.19 (\pm 0.66) + 1.40 (\pm 0.21) \log(M_s/V_s^2 d). \quad (4)$$

This equation is compared to the data in Fig. 1. The solid line shows the fit, and the dashed lines show the one sigma (standard error) confidence limits. One data point (model 12, Table A1) appears as an outlier and might be affected by resonance or the residual effects of a spiral shell.

The numerical results of the simulations show no additional variation of $K_n - 1$ with the second parameter of equation (3). This is illustrated in Fig. 1 using different symbols to denote different values of $1 + M_p/M_s$, which range from 1.75 to 7.0 (for $M_s = 0.25$ – $2.0 M_\odot$ and $M_p = 1.5 M_\odot$). It can be seen that all points follow essentially the same curve. We can set an approximate upper limit on the influence of this parameter by including it in the argument to the power law fit as $GM_s/V_s^2 d \times (1 + M_p/M_s)^\alpha$. We find that $\alpha = -0.29 \pm 0.48$ (or -0.10 ± 0.33 if we omit the outlier) indicating little or no dependence on the second parameter, and therefore little or no dependence on the primary mass. Thus, even though the simulations were made for a single value of M_p ($1.5 M_\odot$), we can expect roughly similar results for other values of M_p in the relatively small mass range (~ 0.6 to a few M_\odot) relevant to stars in the later stages of the AGB.

We conclude that equation (4) gives the main parametric dependence of the envelope shape on the binary parameters in the regime of interest, and we adopt this relation for the remainder of the paper. The dispersion of the model points, characterised by the median deviation, is 0.19 dex. This translates into a dispersion of the observed column density contrast ($C_N - 1$ see below) of $\sim 25\%$. Factors which may contribute to the dispersion are discussed in appendix A. To show the dependence of $K_n - 1$ on individual parameters, Fig. 2 plots equation (4) as a function of d , for fixed values of M_s and V_s , and the model points scaled to these

values using the equation. Figure 3 shows a similar plot as a function of V_s , for fixed M_s and d . Although the relations are not tightly constrained, it can be seen that they are sufficiently well determined to allow a preliminary investigation of the shaping.

The above results are in accord with the discussion by MM99. They found that the quantity R_{acc}^1/d is useful for distinguishing different morphological types of envelopes, where R_{acc}^1 is an effective accretion radius ($= 2GM_s/V_s^2$) using the velocity of the wind at the secondary. Although R_{acc}^1/d has a strict physical interpretation in terms of accretion only in the limit $V_o \ll V_s$, the parameterisation of M_s , V_s , and d is the same as in equation (4) above. MM99 also noted that an analytic formula for the ratio of the accretion rate to the mass loss rate, called α_{focus} by Han et al. (1995) and used by them to characterise the degree of focusing, is, in fact, only a fair indicator of the morphological type. α_{focus} may be written as $(GM_s/d)^2/V_s V_r^3$, where V_r is the relative velocity of the wind at the location of the secondary ($V_r^2 = V_o^2 + V_s^2$). In the limit $V_o \ll V_s$, α_{focus} reduces to a parameterisation equivalent to equation (4), but in the general case it differs. We find that a power law fit of α_{focus} to $K_n - 1$ is a poorer predictor of the density contrast than equation (4), with a dispersion ~ 0.12 dex larger. Equation (4) is therefore the preferred relation. More extensive simulations over a larger range of parameter space are needed to investigate this further.

3.3 Observed shapes

The final step in making the complete connection between the binary properties and observations, is to relate the intrinsic shapes of the envelopes (given above by $K_n - 1$) to the observed shapes. This involves a dependence on the orientation of the envelope, which we take to be the inclination angle (i) of the symmetry axis to the line of sight, and on the kind of observation. For example, it may depend on the distribution of column density, emission measure, or some other quantity, projected onto the plane of the sky.

3.3.1 Column density

We first consider the case where the observed intensity depends on column density. This is relevant to imaging the envelope in optically thin, dust scattered ambient Galactic light, and other techniques such as infrared imaging or millimetre molecular line observations which can be used to determine the column density. We characterise the observed shape of the envelope by the ratio between the column density on the projected major and minor axes at the same distance from the centre, i.e., $C_N = N_{maj}/N_{min}$. It is then straightforward to show that for an edge-on ($i = 90^\circ$) envelope:

$$C_N(90) = \ln K_n K_n / (K_n - 1). \quad (5)$$

This relation is shown as the solid line in Fig. 4. Highly non-spherical envelopes with large values of K_n appear flattened, with $C_N(90) \sim \ln K_n$; and nearly spherical envelopes with values of K_n close to 1, appear nearly circular with $C_N(90) \sim 1$.

For other inclination angles, $C_N(i)$ has been evaluated numerically. The results for several values of K_n are shown

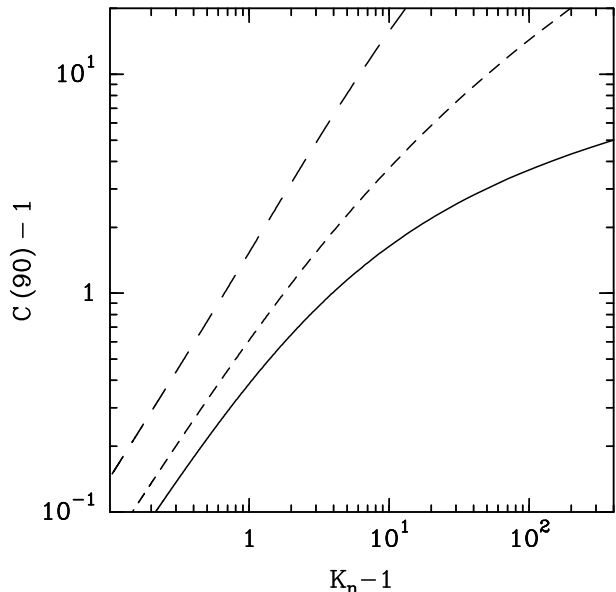


Figure 4. Relation between shape parameter $K_n - 1$ and intensity contrast on the major and minor axes for envelopes seen edge-on ($i = 90^\circ$). Solid line: C_N (intensity \propto column density). Long dashed line: C_E (intensity \propto emission measure). Short dashed line: C_S (scattered central illumination).

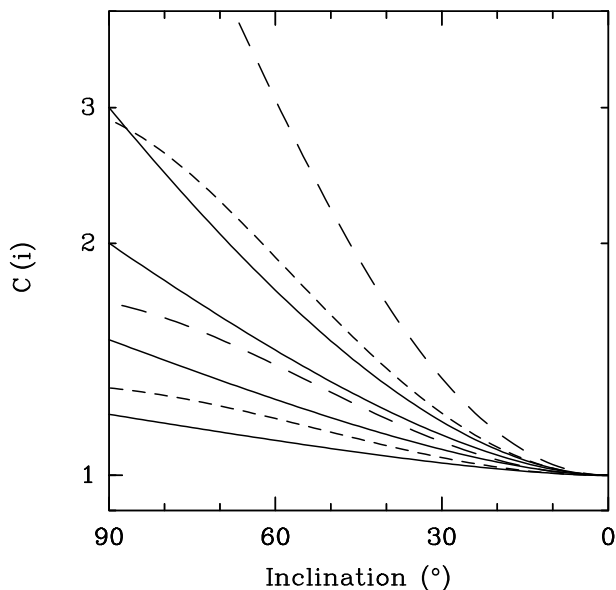


Figure 5. Intensity ratio of envelopes as a function of inclination angle. Solid lines: C_N for values of $K_n = 1.5, 2.0, 4.9,$ and 16.8 (bottom to top). Long dashed lines: C_E . Short dashed lines: C_S . For C_E and C_S , $K_n = 1.5$ and 4.9 .

by the solid lines in Fig. 5. In each case $C_N(i)$, given by equation (5) for $i = 90^\circ$, decreases with decreasing inclination and reaches 1 (i.e., the envelope appears circular) when the system is seen face-on.

We now have a prescription for the observed shape of an envelope formed by gravitational focusing in a binary system. Given the binary parameters M_s , V_s , and d , equation (4) determines the intrinsic structure of the envelope, equa-

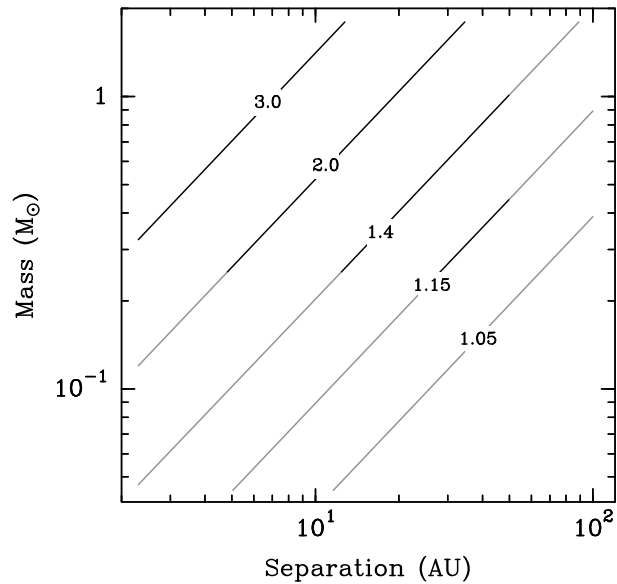


Figure 6. Intensity ratio $C_N(90)$ (intensity \propto column density) of envelopes seen edge-on, as a function of the secondary mass and separation for $V_s = 10 \text{ km s}^{-1}$. The light contours represent regions beyond the parameter range of the simulations.

tion (5) gives the shape seen edge-on, and Fig. 5 shows how this appears at other inclinations.

For later reference, Fig. 6 shows the variation of $C_N(90)$ (the edge-on case) in the secondary mass–separation plane for a representative value of V_s (10 km s^{-1}). Lighter lines are used to extend the contours beyond the actual range of the models (Table A1), assuming that equation (4) remains valid. The velocity of 10 km s^{-1} is the typical terminal velocity of an AGB wind. For small separations, the velocity at the secondary will be less than this (depending on the wind acceleration curve) and the values of C_N will be correspondingly larger; the results of specific cases can be calculated using the equations given.

3.3.2 Emission measure

If the image intensity depends on some quantity other than the column density, the observed shape will in general be different. A dependence on emission measure arises when the AGB halo of a newly formed PN is photo-ionised, and is imaged in the continuum or an emission line whose intensity depends on $\int n^2 dl$ along the line of sight. For this case it may be shown that C_E , the intensity ratio on the projected major and minor axes, is related to the shape parameter K_n by:

$$C_E(90) = \ln K_n^2 \frac{K_n^2 (1 + 4(\ln K_n / \pi)^2)}{K_n^2 - (1 + 8(\ln K_n / \pi)^2)}, \quad (6)$$

for an envelope seen edge-on ($i = 90^\circ$). This relation is shown as the (long) dashed line in Fig. 4. It can be seen that imaging which depends upon emission measure produces a higher contrast than column density, because of the increased sensitivity to the density. The variation of C_E with inclination angle has been evaluated numerically and is found to be similar in form to the curves for C_N . Two examples are shown in Fig. 5.

The shapes of non-spherical AGB halos around PNe are expected to vary over time. When the envelopes become photo-ionised, gradients in the gas pressure will produce flows that tend to smooth out any density gradients (Mellema & Frank 1995). The smoothing time scale at radius r is $t \sim r/v_s$ where v_s is the sound speed in the gas. For $v_s = 10 \text{ km s}^{-1}$, t ranges from 3,000 to 30,000 yr for radii of 10^{17} to 10^{18} cm, which are the size scales typically accessible to observations. Thus contrast in precursor AGB envelopes will still be present in the AGB halos of newly formed PNe, but will eventually disappear in more evolved nebulae.

3.3.3 Central illumination

A variety of other cases can arise when the envelope is observed in dust-scattered light which originates from the central star or nebula. The simplest situation is optically thin, isotropic scattering which may be a reasonable approximation for some halos of proto-PNe and PNe where local absorption effects are not dominant. Other cases, in which the absorption of the radiation from the centre plays an important role, need to be considered on a case-by-case basis. The principles, however, are the same as for those already discussed.

For the optically thin scattering case, it may be shown that C_S , the intensity ratio on the projected major and minor axes, is related to the shape parameter K_n for an envelope seen edge-on ($i = 90^\circ$) by:

$$C_S(90) = \ln K_n \frac{K_n (1 + (\ln K_n / \pi)^2)}{K_n - (1 + 2(\ln K_n / \pi)^2)}. \quad (7)$$

This relation is shown as the (short) dashed line in Fig. 4. It lies between the column density and emission measure curves. The variation of C_S with inclination angle has been evaluated numerically, and two examples are shown in Fig. 5. It can be seen that they are similar in form to the curves for C_N .

For both the scattering and the emission measure cases, figures equivalent to Fig. 6 can be generated by replacing the contour values of C_N with the equivalent values of C_E and C_S found in Fig. 4, or directly by combining equations (6) and (7) with equation (4).

In the cases where dust plays a role in the observations, we have implicitly assumed that the dust/gas ratio is constant throughout the envelope. In fact, there is expected to be a latitude variation in the dust-gas drift velocity because of the variation in density, and this will produce differences between the dust and gas envelopes. There are currently only limited observations bearing on the question of dust-gas coupling in AGB envelopes (e.g., Mauron & Huggins 2000), but it will need to be taken into account in detailed studies. It should not affect that main conclusions of the present paper.

4 DISCUSSION

4.1 Probing the presence of companions

The prescription given above for the large scale shaping of AGB envelopes by binary companions is potentially useful in a variety of situations because the envelopes can be observed with different techniques at optical, infrared, and millimetre

wavelengths; they can also be traced in the halos of proto-PNe and PNe.

In principle, the envelopes of AGB stars with known companions could be used to check the simulations, but in practice there are currently no useful observations available for this purpose. In the case of Mira, which first comes to mind, the envelope appears to be completely disturbed, from the outside by high velocity interaction with the interstellar medium (Martin et al. 2007), and from the inside by the action of bipolar jets (Josselin et al. 2000; Meaburn et al. 2009). For other known binaries, there are no suitable observations of the extended, undisturbed, envelopes. We therefore proceed on the basis that the simulations are correct, bearing in mind that the prescription can be updated when additional information becomes available.

One type of application is the analysis of survey observations of the shapes of AGB envelopes in which the orientation of any binary contribution is unknown. In this case, population syntheses based on random orientations and assumed distributions of companion masses and separations will be needed to evaluate the effects on the observed shapes. Thus the inclination can be accounted for statistically. Since the median inclination for random orientations is 60° , Fig. 5 shows that the shaping signal is well preserved for part of the population under these conditions.

A second type of application is the analysis of individual systems in which the orientation of a possible underlying binary system is already suggested by observations of other structures such as bipolar flows. In this case the inclination can be directly taken into account, e.g., using the curves of Fig. 5. Examples of this approach are given in the sections that follow.

It is interesting to note that the gravitational focusing expressed by equation (4) will respond to changes in the parameters during evolution on the AGB. For example, an increase in the wind velocity and an increase in separation due to mass loss leads to a secular decrease in the degree of flattening of the envelope. This effect offers diagnostic possibilities, but is currently beyond observational capabilities. The sudden transition from quasi-spherical to axi-symmetry during PN formation (see Section 4.3), is attributable to other physical effects.

4.2 IRC+10216

As an illustration of our approach we consider the envelope of IRC+10216, the nearest AGB star with a high mass loss rate. The envelope has been extensively mapped in the millimetre lines of CO and other molecular species (e.g., Huggins et al. 1988; Fong et al. 2006), and it has been imaged at high resolution in dust scattered galactic light (Mauron & Huggins 1999, 2000; Leão et al. 2006). These different observations all show that the extended envelope (10–200'') is roughly circularly symmetric.

In the centre of the envelope on arc-second size scales, HST observations reveal a bipolar structure which is thought to represent the early development of axi-symmetry which characterises the transition to the proto-PNe phase (Skinner et al. 1998; Mauron & Huggins 2000). If a companion is the cause of the bipolarity, it must have been present during ejection of the entire circumstellar envelope.

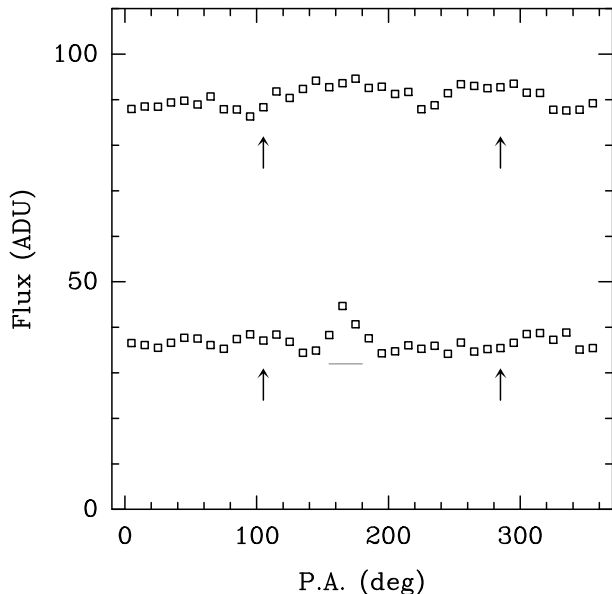


Figure 7. The envelope of IRC+10216: intensity vs. position angle for annuli of radii 10–20'' (top), and 40–50'' (bottom). The horizontal line near 165° marks a region in the data affected by the halo of a bright field star. The arrows indicate P.A.s orthogonal to the bipolar axis; no systematic equatorial enhancement is seen.

The shape of the envelope can therefore be used to probe the presence of the companion.

4.2.1 IRC+10216: envelope shape

We quantify the large scale shape of the envelope using observations of dust-scattered, ambient Galactic light. Away from the centre, the scattering optical depth is small, and the imaging provides an excellent probe of the projected envelope shape. The observations we use were made in the V band with the VLT (FORS1 program 64.L-0204, PI: de Laverny). The data were previously described by Leão et al. (2006), (see also Huggins & Maun 2002), and the processed image is seen in their Figs. 3 and 4. The scattered light images of IRC+10216 show substructure in the form of multiple arcs which have previously been discussed in detail (Maun & Huggins 2000). We are interested here in the large scale geometry averaged over the substructure.

After stars and galaxies were filtered from the image, the envelope was divided into a series of annuli, 10'' in width and centred on the star. The annuli were further divided into 10° bins in position angle. The pixels in each bin were then averaged to determine the envelope intensity above the background. The results are shown in Fig. 7 for two annuli which were the least affected by the halos of bright stars in the field. The formal errors in the intensity are comparable to the symbol size. The radial dimensions of the annuli are 10–20'' and 40–50''; for a distance of 120 pc (Loup et al. 1993) and an expansion velocity of 14.1 km s⁻¹ (Huggins & Healy 1986), they sample the envelope geometry on time scales of 400–2000 yr.

4.2.2 IRC+10216: limits on a companion

The bipolar structure at the centre of IRC+10216 lies at a projected position angle of $\sim 15^\circ$, and from modelling by Skinner et al. (1998) the inclination to the line of sight is $70^\circ \pm 10^\circ$. The expansion time scale for this feature is ~ 50 yr, so it is very recent (Maun & Huggins 2006). If it is caused by interaction with a companion, the companion must have been present during the ejection of the more extended envelope sampled in Fig. 7.

The inclination angle of the bipolar axis means that the system is seen close to edge-on. There is, however, no evidence for enhanced emission on the projected equator (indicated by the arrows in the Fig. 7). Although some of the arc fine-structure deviates from circularity, the average distribution of matter seen in the figure is relatively constant with position angle. The intensity ratio between the equator and the bipolar axis is close to 1. Even after allowing for the inclination, $C_N \lesssim 1.1$.

Reference to Fig. 6 shows that these results place stringent constraints on any hypothesised companion to IRC+10216. For example, if the bi-polarity is caused by the onset of interaction with a companion initially within ~ 10 AU of the primary, the possibility that it can be a stellar object of mass $\gtrsim 0.1 M_\odot$ appears to be ruled out, otherwise the envelope would exhibit observable large scale asymmetry. This result is even stronger when one considers a lower value of V_s appropriate for small separations, rather than the nominal 10 km s⁻¹ used for Fig. 6.

Because of the low limit of C_N , Fig. 6 also shows that even at distances larger than 10 AU from the primary, the mass of any companion is still stringently constrained.

4.3 Binary interaction in the PN transition?

A similar situation is seen in PNe and proto-PNe where the axi-symmetric structure of the nebulae is often surrounded by an extended halo, which is identified with earlier mass loss of the star on the AGB. Numerous examples are seen in the survey observations of Corradi et al. (2003) and Sahai et al. (2007). On the largest size scales the dominant shaping effect of halo gas is interaction with the interstellar medium (e.g., Wareing et al. 2007). Closer to the star the halo shape is expected to reflect the mass-loss geometry on the AGB. It can therefore place important constraints on the origins of bipolar structure in the nebulae, and we discuss this below. It is notable that the PNe with known close companions lack halos (Bond & Livio 1990), which suggests that these form before the late stages on the AGB.

4.3.1 Halo shapes

There is little detailed information on the intrinsic shapes of halos, but they must typically be close to spherically symmetric. There are few, if any, that appear flattened, and they appear round in projection even when the axi-symmetric structure at the centre is seen close to edge-on. The equatorial tori, which often form part of the structure of PNe, do not extend into the halos, and there is good evidence that the tori develop on relatively short time scales along with the axi-symmetry and jets (Huggins 2007).

In the case of evolved PNe, where the nebula is completely photo-ionized by the central star, the gas pressure may play a role in the evolution of the shape of the halo, as described in Section 3.3.2. This effect is less important on shorter time scales, and unimportant in proto-PNe, before the onset of ionisation. Hence the shapes of the halos of proto-PNe provide direct information on the geometry of the mass loss before the nebula forms.

In a recent HST imaging survey of proto-PNe, Sahai et al. (2007) found that the majority (70%) of the 23 objects observed have detectable halos with discernible shapes. Essentially all of these have axi-symmetric structures in their central regions. Most of the halos (75%) are observed to be round. The remainder appear elongated along the bipolar axes of the central structure and are most probably illuminated by (or through) the bipolar lobes; in these cases the overall geometry of the halo is not revealed, but is consistent with spherical symmetry and non-uniform illumination. Thus the sample as a whole provides evidence that mass loss before the onset of axi-symmetry, is mostly spherically symmetric.

In order to quantify the shapes of the halos we have examined the images reported by Sahai et al. (2007) of several proto-PNe, in which the bipolar structure at the center has a considerable inclination angle to the line of sight, as evidenced by their detailed shapes and absorption lanes. These include IRAS 13357–6442, IRAS 17440–3310, IRAS 18420–0512, and IRAS 19475+3119. We characterise the observed shapes of the halos using the intensity ratio at equal distances from the center on axes aligned with the projected equatorial and polar axes of the central bipolar structure (avoiding diffraction spikes, jets, etc.). These ratios, which correspond to C_S in section 3.3.3, all lie in the range 0.6–1.2. The measured uncertainties are $\lesssim 15\%$, and there is good agreement between the results obtained from images with different filters. The individual inclination angles are not known, but they are large by selection (see above). It is reasonable to assume that they are typically $\gtrsim 60^\circ$; using the inclination calculations of section 3.3.3 we can set an upper limit for the edge-on value of C_S of $\lesssim 1.5$. The corresponding column density ratio C_N is ~ 1.3 . There is no evidence for any substantially flattened halos lying in the equatorial plane of the central bipolar structures.

The typical size scale sampled in these halo observations is $\sim 10^{17}$ cm. For a typical halo velocity of 10 km s^{-1} the corresponding expansion age is ~ 3000 yr. The ages of the central bipolarity are typically less by factors of ~ 5 –10 on account of the smaller radial extents and larger expansion velocities. Such rapid time scales are consistent with detailed studies of other proto-PNe where the velocities and inclination angles are known (e.g., Huggins 2007).

4.3.2 Limits on companions

The approximate spherical symmetry of proto-PN halos and the sudden development of axi-symmetry in their inner regions is striking, and can be used to constrain formation scenarios involving binary companions.

The scenarios which have been proposed can be divided into two general types. In the first, the formation of axi-symmetry and jets in the AGB-PN transition is the result of relatively close interaction of the primary

with a companion, e.g., tidal spin-up by the companion, or engulfment followed by envelope spin-up or ejection (e.g., Soker & Livio 1994; Reyes-Ruiz & López 1999; Nordhaus & Blackman 2006). This type of interaction can give rise to an event with short time scales, consistent with observations (Huggins 2007). In the second type of scenario, the components interact via accretion of the AGB wind by the secondary, which produces jets (e.g., Morris 1987; Soker & Rappaport 2000). In this case the jets may be triggered by enhanced mass loss from the primary which produces enhanced accretion by the secondary (Huggins 2007).

In either case, the relative sphericity of the mass loss before the sudden PN event severely constrains the mass and separation of any companion. For example, at separations ~ 10 AU, Fig. 6 shows that for our nominal and conservative limit on asphericity of 1.3, the effect of focusing alone places an upper limit of $\sim 0.2 M_\odot$ on the mass of the secondary. This conclusion is not an artifact of our data fitting. Models 13 and 18 (Table A1) with secondary masses $M_s = 0.25 M_\odot$ and separations 6.3 and 12.3 AU, both have envelopes with large ($\gtrsim 3$) equator-to-pole density ratios and could readily be distinguished as non spherically symmetric. The upper limit on the mass is even more stringent if one considers a more realistic (lower) value for V_s than the nominal 10 km s^{-1} used for Fig. 6. In addition, for very close encounters, other effects are expected to enhance or dominate mass loss in the equatorial plane. These include the influence of tidal effects on the mass loss of the AGB star (Frankowski & Tylenda 2001), and the possible formation of circumbinary disks (Van Winckel 2007; see also Frankowski & Jorissen 2007).

The implications of the absence of flattened halos in proto-PNe and PNe seem inescapable. If relatively nearby binary companions are the cause of the sudden development of axi-symmetry and jets during PN formation, they must typically involve low mass stellar or sub-stellar companions. Only low mass objects may be present at these distances from the primary without the tell-tale shaping of the extended envelope; their effect remains invisible until some interaction with the primary causes a sudden and major change in the mass loss geometry. Even at distances as large as 20–30 AU the absence of observable shaping of the halo constrains the companion mass $\lesssim 0.3$ – $0.5 M_\odot$, according to our nominal criterion. In fact it is an interesting and open question whether a companion can avoid significantly affecting the large scale shape of the AGB envelope by gravitational focusing, and at the same time accrete enough material to generate jets that initiate a transition to strong axi-symmetry. This point is currently under further investigation.

These findings depend, of course, on the applicability of the underlying simulations. Those used (MM99) are the most detailed and comprehensive currently available. It is possible that effects not included in the simulations such as time variable mass loss (evident in the examples discussed above) or the dynamical role of magnetic fields (e.g. Vlemmings et al. 2002; Huggins & Manley 2005; Sabin et al. 2007) may affect the shaping at a quantitative level. Thus updated simulations exploring such effects, and detailed comparisons with observations of AGB stars with companions will be important developments for the future.

5 CONCLUSIONS

This paper shows how the large scale geometry of AGB envelopes can be used to probe the presence of unseen binary companions. The presence of a companion influences the AGB mass loss by focusing it towards the orbital plane. The effect is frozen into the wind at the terminal velocity, and so determines the shape of the envelope at large distances from the star.

We have developed a prescription for the magnitude of the shaping effect, based on the binary simulations of MM99. The prescription provides a tool for the analysis of envelope images at optical, infrared, and millimetre wavelengths. In its present form it has a number of limitations. Most important is the limited parameter space covered by the simulations. It also uses approximations to characterise the intrinsic shapes (Section 3.1) and in relating these to the binary parameters (Section 3.2). These can certainly be refined in the future with the help of more extensive exploration of parameter space.

Using the prescription, we have investigated the commonly observed transition from spherically symmetric mass loss on the AGB to axi-symmetry with jets in proto-PNe and PNe. If this transition is caused by interaction of the primary with a companion, the absence of shaping effects in the extended envelope (or halo) places strong constraints on the mass and separation of the companion. Only low mass objects can orbit close to the primary without observable effects on the envelope shape: they remain invisible until interaction with the primary causes a sudden change in the geometry and dynamics of ejection.

ACKNOWLEDGEMENTS

We thank A. Gruzinov for helpful discussions, and A. Frank and the referee, A. Zijlstra, for comments on the manuscript. This work was supported in part by NSF grant AST 08-06910.

This paper has been typeset from a $\text{\TeX}/\text{\LaTeX}$ file prepared by the author.

REFERENCES

- Bond H. E., Livio M., 1990, *ApJ*, 355, 568
 Chiu P.-J., Hoang C.-T., Dinh-V-Trung, Lim J., Kwok S., Hirano N., Muthu, C., 2006, *ApJ*, 645, 605
 Corradi R. L. M., Schönberner D., Steffen M., Perinotto, M., 2003, *MNRAS*, 340, 417
 de Marco O., 2006, in Barlow M. J., Mendez R. H., eds, *Planetary Nebulae in our Galaxy and Beyond*, IAU Symp. 234, CUP, Cambridge, p. 111
 Fong D., Meixner M., Sutton E. C., Zalucha A., Welch W. J., 2006, *ApJ*, 652, 1626
 Frankowski A., Tylenda R., 2001, *A&A*, 367, 513
 Frankowski A., Jorissen A., 2007, *Baltic Astronomy*, 16, 104
 Gawryszczak A. J., Mikołajewska K., Różycka M., 2002, *A&A*, 385, 205
 Han Z., Podsiadlowski P., Eggleton P. P., 1995, *MNRAS*, 272, 800
 Huggins P. J., 2007, *ApJ*, 663, 342
 Huggins P. J., Healy A. P., 1986, *ApJ*, 304, 418
 Huggins P. J., Manley S. P., 2005, *PASP*, 117, 665
 Huggins P. J., Mauron N., 2002, *A&A*, 393, 273
 Huggins P. J., Olofsson H., Johansson L. E. B., 1988, *ApJ*, 332, 1009
 Josselin E., Mauron N., Planesas P., Bachiller R., 2000, *A&A*, 362, 255
 Jorissen, A. 2003, in Habing H. J., Olofsson H., eds, *Asymptotic giant branch stars*, Springer, Berlin, p. 461
 Leão I. C., de Laverny P., Mékarnia D., de Medeiros J. R., Vandame B., 2006, *A&A*, 455, 187
 Loup C., Forveille T., Omont A., Paul J. F., 1993, *A&A Supp.*, 99, 291
 Martin D. C., et al., 2007, *Nature*, 448, 780
 Mastrodemos N. 1998, Ph.D. Thesis,
 Mastrodemos N., Morris M., 1999, *ApJ*, 523, 357 (MM99)
 Mauron N., Huggins P. J., 1999, *A&A* 349, 203
 Mauron N., Huggins P. J., 2000, *A&A*, 359, 707
 Mauron N., Huggins P. J., 2006, *A&A*, 452, 257
 Meaburn J., Lopez J. A., Boumis P., Lloyd M., Redman, M. P., 2009, arXiv:0903.1966
 Mellema G., Frank A., 1995, *MNRAS*, 273, 401
 Miszalski B., Acker A., Moffat A. F. J., Parker Q. A., Udalski A., 2009, arXiv:0901.4419
 Morris M., 1987, *PASP*, 99, 1115
 Morris M., Sahai R., Matthews K., Cheng J., Lu J., Claussen M., & Sánchez-Contreras C., 2006, in Barlow M. J., Mendez R. H., eds, *Planetary Nebulae in our Galaxy and Beyond*, IAU Symp. 234, CUP, Cambridge, p. 469
 Nordhaus J., Blackman E. G., 2006, *MNRAS*, 370, 2004
 Reyes-Ruiz M., López J. A., 1999, *ApJ*, 524, 952
 Sabin L., Zijlstra A. A., Greaves J. S., 2007, *MNRAS*, 376, 378
 Sacuto S., Jorissen A., Cruzalèbes P., Chesneau O., Ohnaka K., Quirrenbach A., Lopez B., 2008, *A&A*, 482, 561
 Sahai R., Morris M., Sánchez Contreras C., Claussen M. 2007, *AJ*, 134, 2200
 Skinner C. J., Meixner M., Bobrowsky M., 1998, *MNRAS*, 300, L29
 Soker N., Livio, M., 1994, *ApJ*, 421, 219
 Soker N., Rappaport S., 2000, *ApJ*, 538, 241
 Theuns T., Jorissen A., 1993, *MNRAS*, 265, 946
 Vlemmings W. H. T., Diamond P. J., van Langevelde H. J., 2002, *A&A*, 394, 589
 Van Winckel H., 2007, *Baltic Astronomy*, 16, 112
 Wareing C. J., Zijlstra A. A., O'Brien, T. J., 2007, *MNRAS*, 382, 1233

APPENDIX A: DETAILS OF THE MODELS

A1 Model parameters

The simulations that we use to relate envelope shape to binary parameters are taken from MM99. Details of the models are given in Table A1. We omit their model 2 which includes the effects of spin-up, and their models 8 and 9 which have wind velocities at the secondary that are much larger than expected in AGB envelopes. Table A1 includes the binary parameters, the density ratio between the orbital

Table A1. Details of the binary and envelope parameters.

Model	M_s (M_\odot)	d (AU)	V_s (km s^{-1})	V_t	$\frac{n(0)}{n(50)}$	$\frac{n(0)}{n(80)}$	θ_o (deg)	K_n
01	1.00	3.7	5	10	25.00	200.00	15.31	356.63
03	1.00	9.5	11	16	3.20	6.60	42.69	8.23
04	1.00	12.6	17	25	2.50	2.90	64.03	4.08
05	1.00	25.3	15	15	1.30	1.48	197.20	1.58
06	2.00	37.9	15	17	1.60	1.94	113.32	2.21
07	1.00	50.5	15	15	1.50	1.70	136.35	1.93
10	1.00	6.3	9	16	4.60	16.00	30.75	18.67
11	1.00	12.6	12	16	1.60	2.00	110.81	2.25
12	1.00	12.3	7	10	32.00	83.00	16.16	262.13
13	0.25	12.3	7	10	2.60	3.20	59.99	4.48
14	1.00	24.6	9	10	1.90	2.70	79.21	3.11
15	0.50	3.7	5	10	7.50	80.00	21.28	68.61
16	0.50	9.5	11	15	1.70	2.60	88.82	2.75
17	0.50	6.3	9	15	2.90	4.00	52.06	5.63
18	0.25	6.3	9	15	2.30	2.60	70.89	3.56

plane and latitudes 50° and 80° , and our estimates of the shape parameters θ_o and K_n discussed in section 3.1.

A2 Relation of envelope shape to binary parameters

The fit of equation (4) to the model data is shown in Fig. 1, together with the one sigma confidence limits. A higher order curve does not significantly improve the fit. There is a clear outlier (model 12, Table A1), so we characterise the scatter by the median absolute deviation, which is 0.19 dex. This translates into a scatter in observed quantities such as the column density contrast $C_N - 1$ (viewed edge-on) of $\sim 25\%$. There are several factors that may contribute to the scatter of the data points in Fig. 1. (1) Limitations in the model calculations, e.g., the influence of finite simulation volumes, and different degrees to which the models reach exact steady state in the far field. (2) Variation of subordinate parameters, including the terminal velocity and details of the wind acceleration curve. (3) Additional physical effects such as residual spiral structure and resonance between the period and the wind crossing time of the orbit. (4) Deviations from the power law of equation (4), which may vary over the parameter space.

The simulation grid is too sparse to explore the parameter space in detail. However, it is possible to check whether the data are consistent with the combination of parameters used in equation (4), by replacing the independent variable with the more general form of $\log M_s + \gamma \log V_s + \delta \log d$. If we fit the whole data set we obtain the solution $\gamma = -2.41 \pm 0.90$ and $\delta = -0.50 \pm 0.30$, and if we omit the outlier we obtain $\gamma = -2.11 \pm 0.68$ and $\delta = -0.81 \pm 0.29$. The latter solution gives significantly smaller residuals and is preferred, but both solutions are consistent with the combination of parameters used in equation (3) and support the analysis of Section 3.2. A more extensive grid of models would be useful to explore the parameter space in detail.

A3 Comparisons

To our knowledge there are no independent simulations that can be directly compared with the detailed results of MM99. The models by Gawryszczak et al. (2002) show roughly similar levels of gravitational focusing, but they involve some important physical differences concerning the geometry of the mass loss and the role of cooling. Unlike the models of MM99, most of those of Gawryszczak et al. (2002) include initially anisotropic mass loss. The one exception is their model G, which has initially isotropic mass loss, with $M_p = 1.0 M_\odot$, $M_s = 0.6 M_\odot$, $V_s = 9 \text{ km s}^{-1}$, and $d = 9.6 \text{ AU}$. From the latitude-density profile of this model, we find that $C_N(90) = 1.4$. This, however, is expected to be an underestimate of the density contrast. Gawryszczak et al. (2002) point out that the absence of radiation cooling in all their models leads to an underestimate of the density enhancement in the equatorial plane because the inflow is partly suppressed by high pressure gas that forms around the secondary. Consistent with this expectation, if we use the binary parameters of model G in equations (4) and (5), we predict a higher contrast ($C_N = 2.4$) as expected. More detailed and extensive cross-checks on the model results would clearly be useful.

A4 Computational domain

The radial extent of the computational domain of the MM99 simulations ranges from $\sim 1 \times 10^{15}$ to 3×10^{16} cm. The radii of the observations of IRC+10216 shown in Fig. 7 are near the upper end of this range, and those of the proto-PNe halos are up to an order of magnitude larger. For envelopes in steady state at the terminal velocity in each direction, the density profile remains constant with increasing radius, as assumed. The gas at large distances from the star is cool and the turbulent velocity (measured in few cases, e.g., Huggins & Healy 1986) is low, so that these should not have significant dispersal effects. To the extent that the simulations have not reached exact steady state at the terminal velocity within the computational domain, there may be residual changes of shape farther out, but these are expected

to be small. Simulations on extended domains are needed to quantify this.